**Autonomous Robots manuscript No.**
(will be inserted by the editor)

# Dynamically Feasible, Energy Efficient Motion Planning for Skid-Steered Vehicles

**Nikhil Gupta · Camilo Ordonez · Emmanuel G. Collins, Jr.**

Received: date / Accepted: date

**Abstract** Recent research has developed experimentally verified dynamic models for skid-steered wheeled vehicles and used these results to derive a power model for this important class of all-terrain vehicles. As presented in this paper, based on the torque limitations of the vehicle motors, the dynamic model can be used to develop payload and terrain-dependent minimum turn radius constraints and the power model can be used to predict the energy consumption of a given trajectory. This paper uses these results along with Sampling Based Model Predictive Optimization to develop an effective methodology for generating dynamically feasible, energy efficient trajectories for skid-steered autonomous ground vehicles (AGVs) and compares the resultant trajectories with those based on the standard distance optimal trajectories. The simulated and experimental results consider an AGV moving at a constant forward velocity on both wood and asphalt surfaces under various payloads. The results show that a small increase in the distance of a trajectory over the distance optimal trajectory can result in a dramatic savings in the AGV's energy consumption. They also show that distance optimal planning can often produce trajectories that violate the motor torque constraints for skid-steered AGVs, which can result in poor navigation performance.

**Keywords** skid-steered vehicles · dynamic modeling · power modeling · motion planning · energy efficient

N. Gupta, C. Ordonez, and E. Collins are with the Center for Intelligent Systems, Controls and Robotics (CISCOR) and the Department of Mechanical Engineering, Florida A&M University-Florida State University, Tallahassee, FL 32310, USA {ng10, co04d}@my.fsu.edu, ecollins@fsu.edu

## 1 Introduction

In recent years, autonomous ground vehicles (AGVs) have played a major role in various fields such as space exploration, military missions, and agricultural work. In the future, they are expected to perform a variety of tasks in unstructured and dynamic outdoor environments with increasing autonomy. However, an AGV has a finite energy supply stored in batteries and/or fuel, which limits its operational endurance. Hence, to enable an AGV to carry out more extensive missions without recharging or refueling, energy conservation is highly important. Some of this conservation may be accomplished by using hybrid power technologies Dyer (2002). However, once the power system on an AGV is chosen, substantial energy conservation may be achieved via energy efficient motion planning.

The motion planning task is commonly based on minimization of the distance traveled or the traveling time and most motion planning algorithms focus on these problems, for example, Perez and Wesley (1979), Schwartz and Sharir (1988), Hwang and Ahuja (1992). However, as this paper highlights, distance minimization can lead to trajectories that have unnecessary energy consumption and/or violate the torque constraints of a vehicle motor, causing poor trajectory tracking. One should note that for constant velocity, as considered in this paper, the minimum time and minimum distance motion planning problems are identical.

Despite its practical significance, to date there is very little published research in the field of energy efficient motion planning for mobile robots. In Barili et al (1995) the concept of vehicle velocity profile is used to save energy for a mobile robot working in environments cluttered with moving obstacles. That energy-savings strategy avoids frequent acceleration and de-

celeration because of the high-energy consumption, but the work was limited to only straight line motion and did not consider more general curvilinear motion. In Mei et al (2004) a more comprehensive approach to energy efficient motion planning for mobile robots is presented. Power models of the robot motors are developed based on a combination of analytical motor models and experimental data. However, the constraints of a dynamic model (e.g., the minimum turn radius constraints considered here) are not considered. Furthermore, the power model is not based upon a dynamic model; hence, the power model is not valid when the vehicle payload or the terrain surface changes, and developing a new model requires a completely new set of experiments.

This paper considers the development of dynamically feasible, energy efficient motion planner for skid-steered AGVs, an important and large class of all-terrain vehicles. A skid-steered vehicle can be either tracked or wheeled and is characterized by two features. First, the vehicle steering depends on controlling the relative velocities of the left and right side wheels or tracks. Second, all wheels or tracks remain parallel to the longitudinal axis of the vehicle and vehicle turning requires slippage/skidding of the wheels or tracks.

The research by Yu et al (2010) has developed an experimentally verified dynamic model for a skid-steered wheeled vehicle. Collins et al (2011) and Yu et al (2011) used these results to derive a corresponding power model. As initially shown in Ordonez et al (2012b), based on the torque limitations of the vehicle motors, the dynamic model can be used to develop payload and terrain-dependent minimum turn radius constraints. The work also presented the usage of the power model to predict the energy consumption of a given trajectory.

Here, the above results along with Sampling Based Model Predictive Optimization (SBMPO), developed by Dunlap et al (2010) and Dunlap et al (2011a), are used to develop an effective methodology for generating dynamically feasible and energy efficient trajectories for skid-steered AGVs. The resultant trajectories are then compared with minimum distance based trajectories, which is a more standard motion planning approach. It should be noted that by using the energy as the cost function, the proposed motion planning task can also be approached by alternative kino-dynamic motion planners based on optimality such as RRT* Likhachev and Ferguson (2009) and Probability Road Maps Karaman and Frazzoli (2011).

The primary contribution of this paper is the development of an effective motion planning strategy for energy efficient trajectories that are dynamically feasible (which for a skid-steered vehicle means that it satisfies a minimum turn radius constraint). The general methodology relies on the formulation and use of an optimistic heuristic corresponding to an energy cost function and is applicable to a wide variety of mobile robots. For skid-steered vehicles, the results of dynamically feasible, energy efficient motion planning are compared with the more standard distance optimal motion planning, revealing the substantial energy savings that can be achieved and the danger of developing infeasible trajectories.

One of the secondary contributions is the further experimental verification of the previously developed dynamic model for skid-steered vehicles under various combinations of payloads, speeds, and terrains. Also, this paper demonstrates that for skid-steered vehicles, minimum turn radius constraints are dependent upon the vehicle payload and the terrain being traversed, but are not very dependent upon the vehicle speed.

The remainder of this paper is organized as follows. Section 2 presents the kinematic, dynamic, and power models for a skid-steered four-wheeled vehicle. Section 3 briefly reviews SBMPO, and then describes the models and methodology for using SBMPO to generate dynamically feasible, energy efficient trajectories. For both wood and asphalt surfaces, Section 4 first presents and discusses the results of experiments for dynamic model verification. It then presents simulation and experimental results that compare dynamically feasible, energy efficient motion trajectories with more standard distance optimal trajectories for several combinations of payloads, surfaces, and speeds. Section 5 presents preliminary simulation results for motion planning on a sloped surface. Finally, Section 6 summarizes the paper and discusses future work.

## 2 Kinematic, Dynamic and Power Models

This section discusses the kinematic, dynamic, and power models of a skid-steered wheeled vehicle that are key to dynamically feasible, energy efficient motion planning and trajectory following control.

### 2.1 Kinematic Model

As shown in Fig. 1, consider a skid-steered wheeled vehicle moving at constant velocity (i.e., $v_y$ and $\dot{\Psi}$ are constant) about an instantaneous center of rotation (I.C.R.). The local coordinate frame, which is attached to the body center of gravity (CG), is denoted by $x-y$, where $x$ is the lateral coordinate and $y$ is the longitudinal coordinate. When a skid-steered wheeled vehi-

cle rotates, the inner side wheels of the vehicle experience longitudinal skidding or slipping depending on the turn radius, while the outer side wheels experience longitudinal slipping. The lateral sliding velocity $v_x$ is relatively small Mandow et al (2007), Martnez et al (2005), Moosavian and Kalantari (2008) and, hence, is neglected ($v_x = 0$). For vehicles that are symmetric about the $x$ and $y$ axes, an ideal symmetric experimental kinematic model of a skid-steered wheeled vehicle Mandow et al (2007) is given by

$$\begin{bmatrix} v_y \\ \dot{\psi} \end{bmatrix} = \frac{r}{\alpha B} \begin{bmatrix} \frac{\alpha B}{2} & \frac{\alpha B}{2} \\ -1 & 1 \end{bmatrix} \begin{bmatrix} \omega_l \\ \omega_r \end{bmatrix}, \tag{1}$$

where $v_y$ is the vehicle velocity in the forward direction, $\dot{\psi}$ is the vehicle angular velocity, $B$ is the vehicle width, $r$ is the wheel radius, $\alpha$ is a terrain-dependent parameter, and $\omega_l$ and $\omega_r$ are the angular velocities of the left and right wheels, respectively. Therefore, the kinematic model of a skid-steered wheeled vehicle of width $B$ is equivalent to the kinematic model of a differential-steered wheeled vehicle of width $\alpha B$.

The kinematic model of (1) is used in the development of the dynamic model described in the next section. In addition, for vehicle control the inverse of this model is used to determine the desired wheel velocities $\omega_l$ and $\omega_r$, given $v_y$ and $\dot{\psi}$.

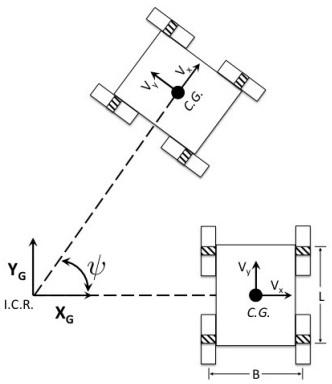


**Fig. 1** A skid-steered vehicle performing a circular turn at constant velocity.

## 2.2 Dynamic Model

The dynamic model was originally presented in Yu et al (2010) and is based on the experimentally verified 'exponential friction model' (Wong and Chiang (2001), Wong (2001)) (i.e., the shear stress varies exponentially with respect to shear displacement) to model the interaction of a skid-steered wheeled robot with the ground. Later, the model was extended to 3D by Ordonez et al (2012b). The model not only gives more accurate predictions of the applied motor torques but is also valid for all turning radii in comparison to models developed using Coulomb friction (in which the shear stress is assumed to be constant) (Caracciolo et al (1999), Kozlowski and Pazderski (2004)), which are valid only for large turning radii. It should be noted that the exponential friction model is accurate only for small accelerations (Yu et al (2010)). However, for energy efficient motion planning, high accelerations and decelerations are generally minimized (Barili et al (1995), Mei et al (2004), Mei et al (2006)). Thus, the model is appropriate for the motion planning task considered here.

In Yi et al (2007), a functional relationship between the coefficient of friction and longitudinal slip is used to present a ground-wheel interaction. The function is further used to develop a dynamic model of skid-steered wheeled vehicle. Also, to enable the robot to follow a desired trajectory, an adaptive controller is designed. The inputs of the dynamic model are the longitudinal slip ratios of the four wheels. However, the longitudinal slip ratios are difficult to measure in practice and depend on the terrain surface, instantaneous radius of curvature, and vehicle velocity. In addition, no experiment is conducted to verify the reliability of the torque prediction from the dynamic model and motor saturation, and power limitations are not considered. In Yi et al (2009), the dynamic model from Yi et al (2007) is used to explore the motion stability of the vehicle, which is controlled to move with constant linear velocity and angular velocity for each half of a lemniscate to estimate wheel slip. As in Yi et al (2007), no experiment is carried out to verify the fidelity of the dynamic model.

Following Yu et al (2010), the dynamic model for a skid-steered wheeled vehicle can be expressed as

$$M\ddot{q} + C(q, \dot{q}) + G(q) = \tau, \tag{2}$$

where $M$ is the mass matrix, $C(q, \dot{q})$ is the resistive term, $G(q)$ is the gravitational term, $q = [\theta_i \ \theta_o]^T$ is the angular position of the inner and outer side wheels respectively, $\dot{q} = [w_i \ w_o]^T$ is the angular velocity of the inner and outer wheels, and $\tau = [\tau_i \ \tau_o]^T$ is the torque of the inner and outer motors. In this work the vehicle is assumed to be moving at constant velocity, which yields $M\ddot{q} = 0$. Also, note that if the vehicle is moving counterclockwise about an I.C.R., then the inner wheel is the left wheel and the outer wheel is the right wheel. The converse is true if the vehicle is moving clockwise about an I.C.R. (i.e., inner = right and outer = left).

The resistive term $C(q, \dot{q})$ of (2) captures the vehicle's ground-wheel interaction, which is based on the

relationship between shear stress $\tau_{ss}$ and shear displacement $j$ given by (Wong and Chiang (2001))

$$\tau_{ss} = p\mu(1 - e^{-j/K}), \tag{3}$$

where $p$ is the normal pressure, $\mu$ is the coefficient of friction, and $K$ is the shear deformation modulus. It is then possible to compute the longitudinal frictional forces on each side of the vehicle by integrating (3) over the contact patch of each wheel (shaded areas in Fig. 1).

The vehicle in Fig. 1 is assumed to have wheels of radius $r$, wheel base $L$, track width $B$, and wheel contact patches of size $p_l \times b$. The contact patches were measured using the Tekscan pressure measurement system (Tekscan (2010)), which employs an array of pressure sensors placed under the tire to generate a profile of its imprint on the surface. Although the actual shape of the contact patch is elliptical, it can be closely approximated by a rectangular shape. This assumption may be violated when the vehicle has large accelerations or if it is moving in rough, 3D environments. These situations are not considered in this paper. In addition, the tire pressure was maintained constant at $20psi$ causing the tire to exhibit negligible deformation for the payloads considered in the study. Therefore, the size of the contact patches can be assumed constant for all experiments. Assuming that the vehicle is symmetric and that it turns with constant angular velocity $\dot{\psi}$ about an instantaneous center of rotation (I.C.R.) (see Fig. 1), it is possible to compute the longitudinal frictional forces for the inner ($F_i$) and outer ($F_o$) sides by integrating (3) over the contact patch area of each wheel such that

$$F_i = \int_{\frac{L-p_l}{2}}^{\frac{L+p_l}{2}} \int_{-\frac{b}{2}}^{\frac{b}{2}} p_{if}\mu_i(1 - e^{-j_{if}/K}) \sin(\pi + \gamma_i) dx_i dy_i + \int_{-\frac{L+p_l}{2}}^{-\frac{L-p_l}{2}} \int_{-\frac{b}{2}}^{\frac{b}{2}} p_{ir}\mu_i(1 - e^{-j_{ir}/K}) \sin(\pi + \gamma_i) dx_i dy_i, \tag{4}$$

$$F_o = \int_{\frac{L-p_l}{2}}^{\frac{L+p_l}{2}} \int_{-\frac{b}{2}}^{\frac{b}{2}} p_{of}\mu_o(1 - e^{-j_{of}/K}) \sin(\pi + \gamma_o) dx_o dy_o + \int_{-\frac{L+p_l}{2}}^{-\frac{L-p_l}{2}} \int_{-\frac{b}{2}}^{\frac{b}{2}} p_{or}\mu_o(1 - e^{-j_{or}/K}) \sin(\pi + \gamma_o) dx_o dy_o, \tag{5}$$

where subscript $o$ and $i$ represent the inner and outer side and subscript $r$ and $f$ represent the rear and front end of the vehicle such that $j_{ir}$ reads as the wheel's shear displacement for the inner-rear side of the vehicle. The variables $\gamma_i$ and $\gamma_o$ denote the angles between the resultant sliding velocities of the inner and outer wheels and the lateral direction of the vehicle. For details on the computation of (4) and (5) please refer to Ordonez et al (2012b).

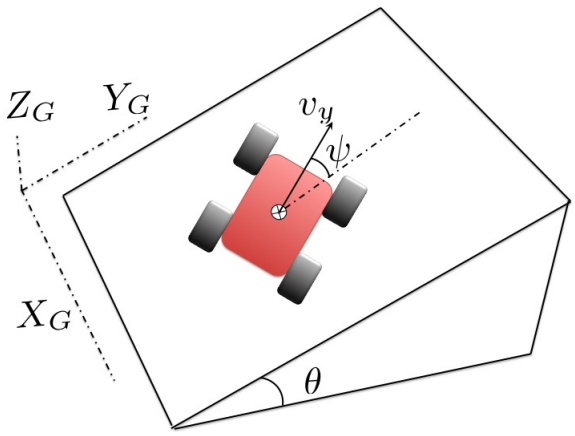


**Fig. 2** Skid-steered vehicle moving on a slopped terrain.

The resistive torque $C(q, \dot{q})$ has an additional component due to the rolling resistance and friction in the motor bearings and other components that make up the drive system. The friction in the drive system $[\tau_{i,res}\ \tau_{o,res}]^T$ is experimentally determined by elevating the robot so that its wheels lose contact with the ground and measuring the motor torques while maintaining a constant linear speed. The rolling resistance forces $[R_i\ R_o]^T$ are determined by measuring the motor torques while the vehicle is moving in a straight line at a constant forward velocity and then subtracting the drive system friction $[\tau_{i,res}\ \tau_{o,res}]^T$.

It follows from the above analysis that the total resistance term $C(q, \dot{q})$ can be expressed by

$$C(q, \dot{q}) = r \begin{bmatrix} F_i + R_i \\ F_o + R_o \end{bmatrix} + \begin{bmatrix} \tau_{i,res} \\ \tau_{o,res} \end{bmatrix}. \tag{6}$$

Furthermore, when traversing slopes as shown in Fig. 2, it is also necessary to overcome the gravitational term $G(q)$, which can be derived by performing a force and moment balance as

$$G(q) = \frac{rW \sin\theta \cos\psi}{B} \left[\frac{B}{2}, \frac{B}{2}\right]^T, \tag{7}$$

where $W$ is the weight of the vehicle, $\theta$ is the slope of the terrain, and $\psi$ is the angular orientation of the vehicle.

For a more detailed explanation of the dynamic model presented here, please refer to Ordonez et al (2012b).

### 2.3 Power Model

This section describes the power model used in the study along with its integration with respect to time to compute the energy consumption of an AGV for a particular trajectory. The model was originally presented

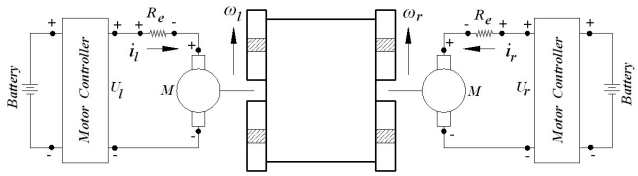


**Fig. 3** The circuit diagram for the left and right side of a skid-steered wheeled vehicle.

in Collins et al (2011),Yu et al (2011) and uses the general dynamic model described in Section 2.2.

The power model, presented in Collins et al (2011), uses separate power models for the left and right side motors. It should be noted that left side wheels are coupled together and mechanically connected to the left side motor. Similarly, the right side wheels are coupled together and connected to the right side motor. The equivalent circuit describing the left and right side drive system and motors can be seen in Fig. 3. The circuit includes a battery, a motor controller, a motor, and the motor electrical resistance $R_e$ for each side of the motor. In Fig. 3, $\omega_l$ and $\omega_r$ are the angular velocities of the left and right wheels, and $i_l$ and $i_r$ are the currents of the left and right circuits. The vehicle is assumed to be turning CCW and have a turning radius larger than half the width of the vehicle so that $\omega_l$ and $\omega_r$ are always positive.

The power model of a DC motor is given by

$$P_m = \omega_m \tau + R_m I_m^2, \tag{8}$$

where $\omega_m$ is the motor angular velocity, $\tau$ is the torque output of the motor, $R_m$ is the motor electrical resistance, and $I_m$ is the current through the motor. The first term on right side of (8) is the mechanical power consumption, which includes the power to compensate the left and right sliding frictions and the moment of resistance along with the power to accelerate the motor, while the second term is the electrical power consumption due to the motor resistance dissipated as heat. It should be noted that this study used DC brushed motors as the vehicle actuators; hence electrical power consumption plays a major role in the power model. However, if different actuators are utilized, one has to change the electrical portion of the power model accordingly.

Using (8) and the motor torque-current relationship, $\tau = K_T i$, the power consumption for the left and right motors $P_l$ and $P_r$, having efficiency $\eta_l$ and $\eta_r$ respectively, can be expressed as

$$P_l = \frac{\tau_l \omega_l}{\eta_l} + (\frac{\tau_l}{K_T g_r \eta_l})^2 R_e, \tag{9}$$

$$P_r = \frac{\tau_r \omega_r}{\eta_r} + (\frac{\tau_r}{K_T g_r \eta_r})^2 R_e, \tag{10}$$

where $K_T$ is the torque constant and $g_r$ is the gear ratio of the motor. Let $P$ denote the power that must be supplied by the motor drivers to the motors to enable the motion of a skid-steered wheeled vehicle and define the operator $\sigma : \mathbb{R} \to \mathbb{R}$ such that

$$\sigma(Q) = \begin{cases} Q: & Q \geq 0 \\ 0: & Q < 0. \end{cases} \tag{11}$$

Then the entire power model of a skid-steered wheeled vehicle is

$$P = \sigma(P_r) + \sigma(P_l). \tag{12}$$

Typically, one might expect to write $P = P_r + P_l$. However, it turns out that $P_l$ can be negative when the torque applied by the left side motor is zero and the left wheel is rotated due to the torque applied to the right wheel and the coupling of the system dynamics. This causes power generation on the left side of the vehicle. The power generated does not charge the battery in our research vehicle, thus the more general form (12) is used. To enable the battery to be charged requires modifications of the motor controller, which was not done in this research. For a more detailed power model please refer to Collins et al (2011).

The above analysis reveals that $P = P(\tau)$, i.e., the total power consumption is a function of $\tau$, the vector of motor torques, which is determined using the dynamic model (2). Given $P(\tau)$, the energy consumption $E$ for the vehicle in the time interval $[t_o \ t_f]$, where $t_o$ is the start time and $t_f$ is the final time, may be computed as

$$E = \int_{t_o}^{t_f} P(\tau) dt. \tag{13}$$

## 3 Sampling Based Model Predictive Optimization (SBMPO)

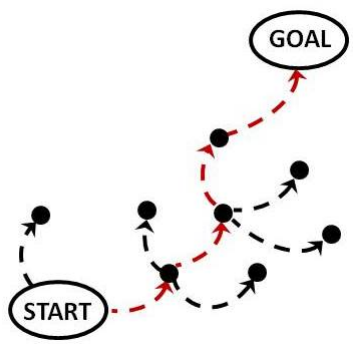


**Fig. 4** Portion of a graph tree resulting from the SBMPO sampling process and model integration.

SBMPO is a sampling-based algorithm for motion planning. It is based on sampling the inputs to a kinematic or dynamic model and integrating the model to build a tree, as illustrated by Fig. 4. A* optimization is used to find the optimal tree path, providing the optimal trajectory based on the cost function provided. SBMPO has been demonstrated as an effective and efficient trajectory planning technique for autonomous underwater vehicles (AUVs) Caldwell et al (2010), ground-based mobile robots Ordonez et al (2012b), Ordonez et al (2013), legged robots Ordonez et al (2012a) and robotic manipulators Chuy et al (2013). The efficiency of SBMPO is closely linked to the development of an appropriate optimistic A* heuristic. Also, Reese (2015) proves the important theorem that "upon termination, the SBMPO algorithm will produce a path of nodes representing the minimal cost trajectory among those represented by the graph." For energy efficient motion planning, this paper describes an optimistic heuristic cost function based on energy that facilitates the efficient computation of energy efficient trajectories.

Fig. 5 shows the block diagram of a trajectory planning strategy that uses SBMPO. The models, cost evaluation, and heuristic are supplied by the user. The inputs to either the kinematic model or dynamic model are sampled and that model is the one integrated by SBMPO. The remaining models (including the obstacle map) are represented as constraints that enable unacceptable states to be eliminated. In the dynamically feasible, energy efficient motion planning considered in this research, a simple kinematic model that maps the longitudinal and angular velocities to the vehicle position and orientation (see Section 3.2) is the integration model and the minimum turn radius constraints (see Section 3.3) represent the dynamic model. The developed strategy can be used for any given mobile platform as long as its kinematic and dynamic models are defined, and its energy cost can be computed for the given path. Preliminary results for applying this strategy to energy efficient motion planning of RHex-type robots is given in Ordonez et al (2012a).

It should be noted that in the SBMPO algorithm, a graph is created from start to goal and each vertex on the graph keeps track of the states of the system, the control input, and cost associated with the state. For detailed information, please refer to Dunlap et al (2010) and Dunlap et al (2011b).

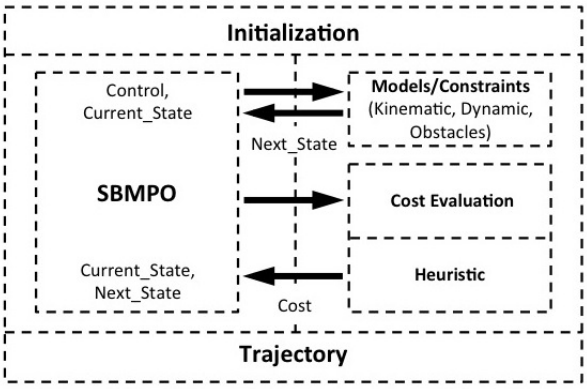


**Fig. 5** Trajectory planning using Sampling Based Model Predictive Optimization (SBMPO).

### 3.1 SBMPO Algorithm

The following are the main steps of SBMPO:

1. *Select a node with highest priority in the queue*: The nodes are collected in an Open List, which ranks the potential expansion by their priority or low cost associated with the node. The Open List is implemented as a heap so that the highest priority node that has not been expanded is on top. If the selected node is the goal, SBMPO terminates, otherwise go to step 2. Note that the node representing the start will have the highest initial priority.
2. *Sample input space*: Generate a sample of the input to the system that satisfies the input constraints. The input sample and current state (i.e., the state of the selected node) are passed to the system model, and the system model is integrated to determine the next state of the system. If the next state satisfies all constraints, then continue to Step 3, else repeat Step 2.
3. *Add new node to the graph*: Use an implicit grid Ericson (2005) to check if the graph already contains a node close to the new state of the system. If such a node exists, only add an edge from the current node (i.e., the selected node) to the node whose state is similar to the new state. Otherwise, add a node whose state is the next state.
4. *Evaluate new node cost*: Use an A* heuristic to evaluate the cost of the generated vertices based on the desired objective (which is least amount of energy). Add a new node to the priority queue based on the minimum cost.
5. *Repeat* $2-4$ *for* $n$ *successors*: Steps $2-4$ are repeated for $n$ successors, where $n$, the *branchout factor*, is defined by the user.
6. **Repeat $1-5$ until one of the stopping criteria is true: Steps $1-5$ are repeated until the goal region is reached or the maximum number of allowable iterations is achieved. It should be noted that though the SBMPO is based on A* search algorithm, once the goal region**

**has been reached, irrespective of unexplored nodes still available in the priority queue, the planner stops. This is done in order to make the SBMPO computationally efficient and effective online. Due to this reason the final path is sub-optimal.**

### 3.2 Model used in SBMPO

Referring to the upper right hand block in Fig. 5, this section discusses the simple kinematic model used by SBMPO. Since, in this study $v_y$ is kept constant, sampling $\dot{\psi}$ and using a simple kinematic model provides the vehicle position in the global space by SBMPO. It is assumed that the vehicle states are sampled with fixed time period $T$. Then, the position $[X_G, Y_G]$ and orientation $\theta_G$ of the vehicle in the global space is given by

$$\begin{aligned} \theta_{G,k} &= \theta_{G,k-1} + \dot{\psi}_k T, \\ X_{G,k} &= X_{G,k-1} + v_y \cos(\theta_{G,k}) T, \\ Y_{G,k} &= Y_{G,k-1} + v_y \sin(\theta_{G,k}) T, \end{aligned} \tag{14}$$

where $k$ is the time index for the current state. SBMPO uses this model to evaluate the vehicle cost and position in the global space for the $\alpha$ corresponding to the surface under consideration.

### 3.3 Dynamic Constraints

**Fig. 6** A skid-steered vehicle (the FSU-Bot) moving on a flat asphalt surface while being tracked by a Vicon motion capture system.

Referring again to the upper right hand block in Fig. 5, this section describes the minimum turn radius constraints derived from the dynamic model. For a given surface, (constant) vehicle speed, and vehicle payload, the dynamic model (2) can be used to generate curves that show the torque of the inner and outer motors as a function of the turn radius Yu et al (2010). Examples of these curves for the FSU-Bot of Fig. 6 are the analytical

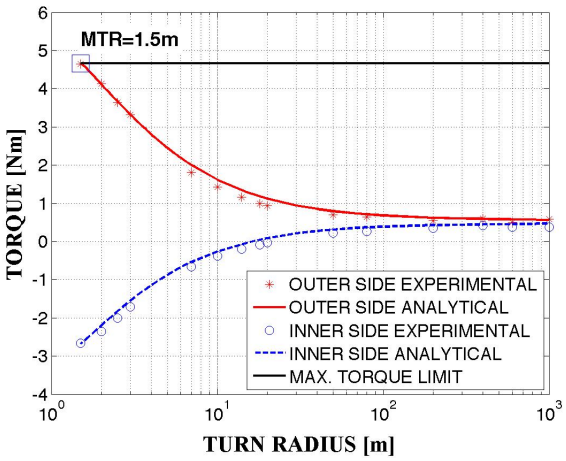


**Fig. 7** Torque vs. Turn Radius curve for the FSU-Bot moving at a constant forward velocity of $0.2m/s$ with no payload on a flat wooden surface. The minimum turn radius ($MTR$) for no payload is $1.5m$.

curves shown in Fig. 7. Since the motors have torque limitations, illustrated by the solid horizontal line in Fig. 7, any turn radius less than the radius corresponding to the intersection of that line and the analytical curve (for the outer side motor) is unachievable. This turn radius is denoted the minimum turn radius (MTR) and is the radius corresponding to the small square in Fig. 7. This results in the constraint

$$R \geq MTR. \tag{15}$$

Note that the MTR will increase as the surface friction or payload increases. Also, for a given skid-steered vehicle, it is possible for the MTR to be zero. For example, this can occur if the motors are sufficiently powerful and the vehicle payload is sufficiently small.

For implementation of the MTR constraint in SBMPO, the turn radii corresponding to the sampled nodes were computed and the nodes corresponding to the infeasible turn radii were rejected. The turn radius between any two nodes (see Fig. 4) is assumed to be constant at the value it has at the child node. (This is an approximation, which is needed for real time implementation.) Let $k$ denote the current time, corresponding to the parent node, such that $k+1$ is the time corresponding to any of the child nodes. Consider the child node corresponding to the $i^{th}$ sample (of $n$ samples). It has angular velocity denoted by $\dot{\psi}_{k+1,i}$ and linear velocity $v_y$ (since it is assumed that the linear velocity is $v_y$ throughout the trajectory). The turn radius between these two nodes, denoted by $R_{k\to k+1,i}$, is then given by

$$R_{k\to k+1,i} = \frac{v_y}{\dot{\psi}_{k+1,i}}. \tag{16}$$

### 3.4 Cost Evaluation and Heuristic for Energy Efficient Planning

The elements of Fig. 5 that must be chosen for energy efficient motion planning are the cost function and the corresponding heuristic. An expression for the energy consumption $E$ has already been given by (13) in terms of $P(\tau)$. However, since $\tau$ depends on the vehicle turning radius $R$ and orientation (in case of slopped terrain), and both vary continuously, it is not generally feasible to perform the integration of (13) in real time.

Referring to (13), let $k = 0$ correspond to $t_o$, the time of the start node, and $k = N$ correspond to $t_f$, the time of the current node. Then the energy cost $E$ for the trajectory from the start node to the current node can be approximated by

$$E = \sum_{k=0}^{N} P_k T, \tag{17}$$

where $T$ is the constant sample time and $P_k$ is the power needed to move from the node at time $k$ to the node at time $k+1$, assuming that, following the derivation of (16), for angular velocity $\dot{\psi}_{k+1}$ and linear velocity $v_y$ the radius of curvature is given by $R_{k\to k+1} = v_y/\dot{\psi}_{k+1}$. For efficient implementation with SBMPO, tables displaying power $P$ vs. turn radius $R$ for various payloads were generated using the dynamic and power model respectively described in Sections 2.2 and 2.3. These tables are then used to determine the power terms $P_k$ in (17) as a function of the turn radius $R_{k\to k+1}$.

The heuristic cost is computed as follows. Let $D$ denote the straight line distance from the current node to the goal node and let $t$ denote the time needed to move the distance $D$ at the linear velocity $v_y$, such that $t = \frac{D}{v_y}$. Then, an optimistic heuristic $H$ is given by

$$H = P_\infty t + mgh, \tag{18}$$

where $P_\infty$ denotes the power consumption corresponding to linear motion (i.e., $R = \infty$) on flat ground, $m$ is the mass of the vehicle, $g$ is the gravity constant, and $h$ is the vertical height of the goal from the vehicle's current position in space. In most of the current study the robot is moving on a flat surface, in which case $h = 0$.

### 3.5 Tuning of SBMPO

As with all motion planning algorithms, SBMPO has parameters that require tuning to obtain efficient use of the algorithm. The primary tuning parameters are the dimension of the implicit grid in Step 3 of Section 3.1 and the branchout factor, defined in Step 5 of that section. Each tuning parameter is non-linearly dependent on the other and can have a significant effect on the computation time. For the implementation of SBMPO used for the motion planning problems described in Section 4, trial and error revealed that a grid size of $0.005m$ and branch out factor of 20 tended to give minimal computation times. Hence, these parameters were used in each of the experiments of Section 4. It should be noted that gridding was only implemented for the x and y axes but not for the heading angle. Gridding of the heading angle may be used if a constraint is required for the final vehicle orientation, which is not the case in this study.

## 4 Results and Discussion

This section compares distance optimal trajectories with the corresponding energy efficient trajectories on two different terrains, plywood[1] (hereafter simply called "wood") and asphalt. The experimental platform is the FSU-Bot, shown in Fig. 8, a skid-steered robot that employs 2 mechanically coupled Pittman GM 9236 brushed DC motors per side. Each pair of motors is controlled using a current control approach by a Maxon motor controller (4-Q-dc). The motor controllers are configured to provide a maximum current of $5A$, which corresponds to a maximum torque of $4.63Nm$. The top plate of the robot was modified to accommodate steel bars of $2kg$ each as shown in Fig. 9. The added weight corresponds to the robot payload and the payloads in the experiments had increments of $4kg$ each; i.e., a $2kg$ bar was added on each side of the vehicle, equidistant from the center. The new modification helped to retain the bars securely without significantly affecting the vehicle's center of mass in the horizontal plane, which made the use of the dynamic model in the experiments more convenient since the center of mass of the vehicle did not have to be recomputed. All experiments were performed at a constant tire pressure of $20psi$. The key parameters of the FSU-Bot are listed in Table 1. The efficiency of the motor is estimated by taking the ratio of average power output to average power input of the motor. The power output of the motor is computed by the force exerted by the rotation of the motor shaft on the spring scale multiplied by the radius of the motor shaft. The product of the applied voltage and current drawn by the motor provided the power input. Though, the efficiency of a DC motor varies with the operating state of the motor, it is assumed to be constant in this study.

[1] A modular wooden surface was used because it can be attached to a variable slope in the authors' lab for future experiments that focus on sloped surfaces

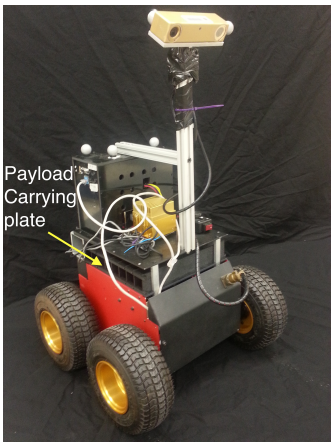


**Fig. 8** The FSU-Bot skid-steered wheeled robot used in the study.

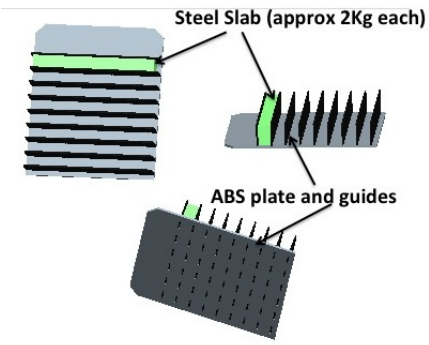


**Fig. 9** The payload carrying plate design for the FSU-Bot used in the study.

**Table 1** Key parameters of the FSU-Bot

| | | |
|---|---|---|
| Vehicle | | |
| Mass (kg) | $m$ | 23.2 |
| Track width (m) | $B$ | 0.39 |
| Wheel base (m) | $L$ | 0.27 |
| Radius of tire (m) | $r$ | 0.1075 |
| Motor | | |
| Torque constant (Nm/A) | $K_T$ | 0.023 |
| Speed constant (rad/sV) | $K_n$ | 43.478 |
| Gear ratio | $g_r$ | 49.8 |
| Motor Electrical Resistance ($\Omega$) | $R_e$ | 0.74 |
| Motor Efficiency | $\eta$ | 0.76 |
| Wooden Surface | | |
| Expansion factor | $\alpha_{wood}$ | 1.44 |
| Outer wheel coefficient of friction | $\mu_o$ | 0.8806 |
| Inner wheel coefficient of friction | $\mu_i$ | 0.5795 |
| Shear deformation modulus (m) | $K$ | 0.0013 |
| Asphalt Surface | | |
| Expansion factor | $\alpha_{asphalt}$ | 1.39 |
| Outer wheel coefficient of friction | $\mu_o$ | 1.2165 |
| Inner wheel coefficient of friction | $\mu_i$ | 0.8269 |
| Shear deformation modulus (m) | $K$ | 0.0016 |

### 4.1 Dynamic Model Verification

The FSU-Bot was commanded to move at $0.2m/s$ constant forward velocity on each surface for various turn radii to estimate the terrain dependent surface parameters for the dynamic model discussed in Section 2.2. A total of 3 runs were performed for each turn radius and the motor torques for the outer and inner vehicle sides were measured by monitoring the current through the motors. The robot with no payload was commanded to move on both the wood and asphalt surfaces. The terrain dependent parameters ($\mu_o, \mu_i$, and $K$) were estimated by fitting (in the least squares sense) the proposed model to the experimental torques (shown in Fig. 7), yielding $\mu_o = 0.8806$, $\mu_i = 0.5795$, and $K = 0.0013$ for the flat wooden surface. It should be emphasized that the surface parameters obtained here were estimated for the no payload case. The solid black line in Fig. 7 represents the maximum torque limit of the vehicle ($4.63Nm$) of one of the vehicle's motors. A Vicon motion capture system was used to track the vehicle motion and estimate the expansion factor as discussed in Section 3.2. For the FSU-Bot moving on the flat wooden surface at $0.2m/s$ with no payload the expansion factor was estimated to be $\alpha = 1.44$. The estimated surface parameters for asphalt were $\mu_o = 1.2165$, $\mu_i = 0.8269$, and $K = 0.0016$ with an expansion factor $\alpha = 1.39$.

**Table 2** Minimum turn radius (MTR) constraint depending on terrain type and payload

| Terrain | Surface Parameters ($\mu_o$, $\mu_i$, $K$) | Payload ($Kg$) | MTR ($m$) |
|---|---|---|---|
| Wood | $(0.8806, 0.5795, 0.0013)$ | 0 | 1.5 |
| | | 4 | 2.0 |
| | | 8 | 2.5 |
| | | 12 | 3.0 |
| Asphalt | $(1.2165, 0.8269, 0.0016)$ | 0 | 2.0 |
| | | 4 | 2.5 |
| | | 8 | 3.0 |
| | | 12 | 4.0 |

Later, using the surface parameters and the expansion factor corresponding to motion with no payload on a wooden surface, the model was used to predict the torques and minimum turn radius dynamic constraints for $4kg$, $8kg$ and $12kg$ payloads. For both the wood and asphalt surfaces, Table 2 summarizes the minimum turn radius dynamic constraints for the FSU-Bot with various payloads. As shown in Figs. 10−12, the model was able to accurately predict the effect of payload on the vehicle torques and the MTR, which is shown by the

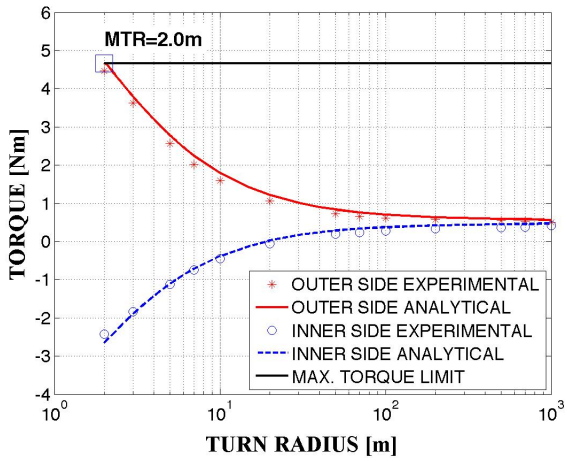


**Fig. 10** Torque vs. Turn Radius curve for the FSU-Bot moving at a constant forward velocity of $0.2m/s$ with $4kg$ payload on a flat wooden surface. The minimum turn radius ($MTR$) for a $4kg$ payload is $2.0m$. (The surface parameters were estimated for no payload, demonstrating good generalization of the model to payload changes.)

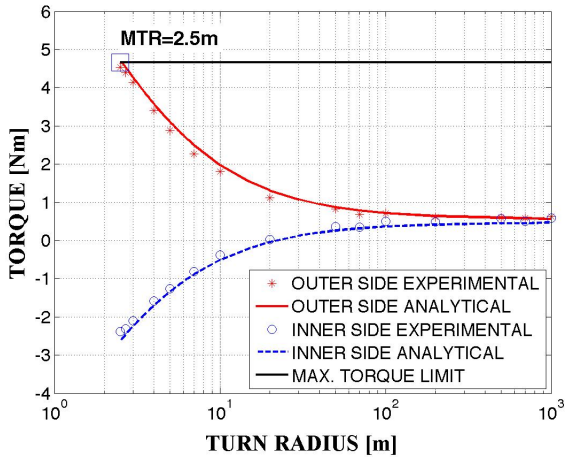


**Fig. 11** Torque vs. Turn Radius curve for the FSU-Bot moving at a constant forward velocity of $0.2m/s$ with $8kg$ payload on a flat wooden surface. The minimum turn radius ($MTR$) for an $8kg$ payload is $2.5m$. (The surface parameters were estimated for no payload, demonstrating good generalization of the model to payload changes.)

$x$-axis value corresponding to the point where the maximum torque line intersects the outer torque prediction curve (shown in Figs. 10−12). For the FSU-Bot with no payload moving on the wooden surface with a constant forward velocity of $0.2m/s$ the predicted MTR is $1.5m$. As shown in Fig. 7, the experimental results verified this value. With the increase in payload, the vehicle's MTR increases. For example, for a $4kg$ payload the predicted and experimental MTR was $2m$ (see Fig. 10), whereas for a $12kg$ payload it turns out to be $3m$ (see Fig. 12).

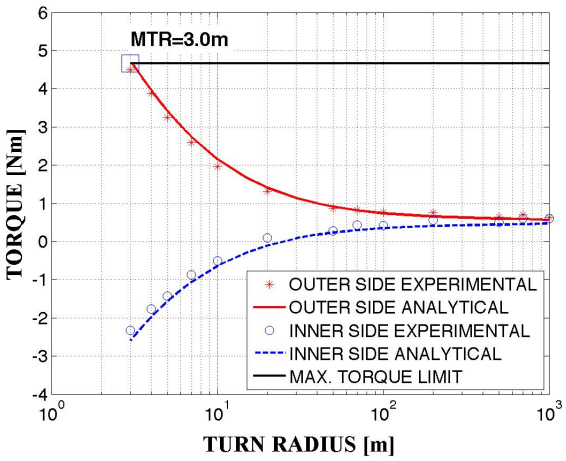


**Fig. 12** Torque vs. Turn Radius curve for the FSU-Bot moving at a constant forward velocity of $0.2m/s$ with a $12kg$ payload on a flat wooden surface. The minimum turn radius ($MTR$) for $12kg$ payload is $3.0m$. (The surface parameters were estimated for no payload, demonstrating good generalization of the model to payload changes.)

### 4.2 Motion Planning Simulation Results

Simulations were performed to compare the distance and energy requirements of dynamically feasible, energy efficient trajectories with those of the corresponding distance optimal trajectories. *Below, "energy efficient motion planning" refers to motion planning that both optimizes an energy cost function and enforces the MTR constraint. Hence, an "energy efficient trajectory" is also dynamically feasible (i.e., it meets the MTR constraint). The simpler language is used for ease of presentation.*

In this research, distance optimal trajectories were computed using SBMPO along with the kinematic model discussed in Section 3.2. The cost function used for distance optimal motion planning was the distance traveled and the heuristic was the Euclidean distance. Since traditional distance optimal motion planning does not exploit the dynamics of the vehicle, no dynamic constraints (i.e., MTR constraints), were considered for those trajectories, such that it was assumed that the vehicle could provide all the actuation required to negotiate a given trajectory's turns. Hence, the trajectories were not all necessarily dynamically feasible, i.e., they may violate the MTR constraints (and often did). However, even in this case, the energy predictions are indicative of the energy consumption of a vehicle that has more powerful motors. These results are important since it appears that skid steered vehicles are sometimes designed with extremely powerful motors for which MTR constraints may not exist under many circumstances (i.e., payloads and terrain surfaces).

The simulations involved various scenarios, characterized by the initial position and orientation of the vehicle, the location of the goal, and the obstacle configuration (if any). However, due to space limitations only three of them are discussed in detail. Statistics based on all of the performed simulations are described at the end of this section. In each simulation, the robot was assumed to move at a constant forward velocity of $0.2m/s$ on a $7m \times 7m$ wooden surface. As shown in Figs. 13−15, the goal region is represented by a solid (blue) circle centered at the goal location and having a radius of $0.3m$. Table 3 shows the computed results for total energy and path length and their comparison.

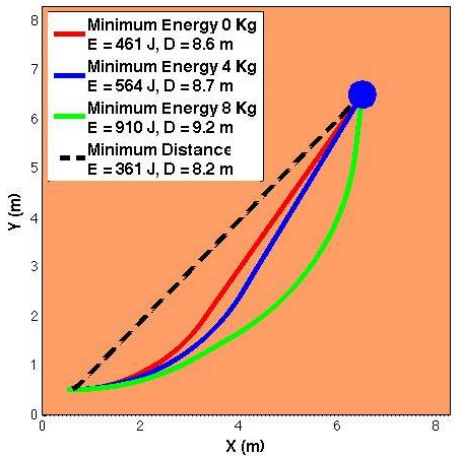


**Fig. 13** Simulated motion planning results for Scenario 1 with 0° initial heading with respect to the $x$-axis, start at $(0.5, 0.5)m$, goal at $(6.5, 6.5)m$, and a constant forward velocity of $0.2m/s$ on a flat wooden surface. The distance optimal trajectory did not change with the variation in payload and always made an initial sharp turn to orient the vehicle towards the goal and minimize the distance. The energy optimal trajectory avoided sharp turns to avoid unnecessary energy consumption. As the payload increased the energy optimal trajectory made wider turns.

The planning is first performed for an obstacle free environment (Scenario 1) using both distance and energy optimization for various payloads. For Scenario 1, the robot was assumed to move from start position at $(0.5, 0.5)m$ with an initial heading direction of 0° with respect to the $x$-axis to the goal region centered at $(6.5, 6.5)m$. As shown in Fig. 13, for distance optimal motion planning the vehicle made a sharp turn in the beginning and then moved in a straight line towards the goal. For no payload energy efficient motion planning, the vehicle avoided sharp turns and moved along an arc towards the goal. However, as the payload increased, the vehicle followed a wider turn. The predicted total energy consumption for the no payload distance optimal trajectory was $361J$, whereas for the

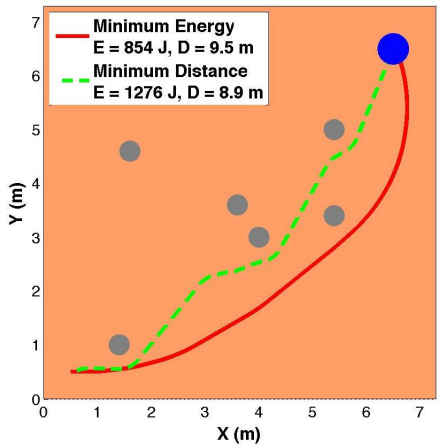


**Fig. 14** Simulated motion planning results for Scenario 2 with 0° initial heading with respect to the $x$-axis, start at $(0.5, 0.5)m$, goal at $(6.5, 6.5)m$, no payload, and a constant forward velocity of $0.2m/s$ on a flat wooden surface. The distance optimal trajectory made sharp turns to minimize the distance to reach the goal. In contrast, the energy optimal trajectory made wide turns to avoid the high energy consumption associated with the sharp turns.

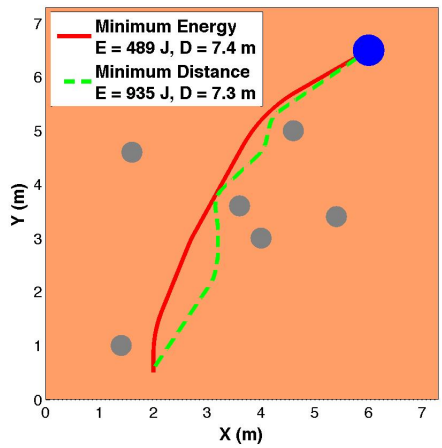


**Fig. 15** Simulated motion planning results for Scenario 3 with 90° initial heading with respect to the $x$-axis, start at $(2.0, 0.5)m$, goal at $(6.0, 6.5)m$, no payload, and a constant forward velocity of $0.2m/s$ on a flat wooden surface. As in Fig. 14, in this scenario also the distance optimal trajectory made sharp turns to minimize the distance to reach the goal. In contrast, the energy optimal trajectory made wide turns to avoid the high energy consumption associated with the sharp turns.

no payload energy efficient trajectory it was $461J$. It should be noted that for the distance optimal motion planning of Scenario 1 the vehicle made a sharp turn (violating the MTR constraint) for a small time and then moved straight for the rest of the trajectory. This resulted into a lower energy consumption as compared to the energy efficient trajectories for various payloads. Energy efficient trajectories made sure that the MTR

**Table 3** Simulation results for motion planning

| Scenario | Planning | Comp. Time (s) | Path Length (m) | Path Difference⋆ (%) | Energy (J) | Energy Difference⋆ (%) |
|---|---|---|---|---|---|---|
| 2. | Min. Dist. | 0.5554 | 8.9 | 6.71 | 1276 | 33.07 |
| | Min. Energy | 0.8798 | 9.5 | | 854 | |
| 3. | Min. Dist. | 0.5664 | 7.3 | 1.35 | 935 | 47.70 |
| | Min. Energy | 0.186 | 7.4 | | 489 | |

⋆The path and energy differences are computed with respect to minimum distance motion planning.

constraint is not violated, which sometimes can result in higher energy consumption compared to a distance optimal trajectory.

Motion planning results for Scenarios 2 and 3 involved obstacles and are shown respectively in Figs. 14 and 15. For Scenario 2, the robot start position was $(0.5, 0.5)m$ with the goal region centered at $(6.5, 6.5)m$. However, for Scenario 3, the robot start position was $(2.0, 0.5)m$ with the goal region centered at $(6.0, 6.5)m$. It should be noted that as mentioned in section 3.1, SBMPO terminates once the goal is reached irrespective of the unexplored nodes still available in the priority queue. Due to this along with the limitation of sampling method the trajectories shown in Figs. 14 and 15 are sub-optimal. Provided the algorithm was made to run till the priority queue is emptied out the trajectories would be more optimal. The corresponding results of Table 3 reveal that for a small increase in distance, the energy based planning is able to dramatically decrease the energy consumption. For example, for Scenario 2 of Fig. 14, a 6.7% increase in distance led to a 33.1% decrease in energy consumption, while for Scenario 3 of Fig. 14, a 1.4% increase in distance led to a 47.7% decrease in energy consumption.

Trajectories were designed for the robot's movement on the $7m \times 7m$ wooden surface for a total of 14 scenarios. The payload was varied from $0kg$ to $12kg$ in increments of $4kg$. The start and goal location of the robot were varied randomly with randomly placed obstacles, varying in number from 2 to 8. The orientation of the robot was selected as either $0°$ or $90°$ with respect to x-axis. In each of the simulation results, the distance optimal motion planning violated the MTR constraint. (It is certainly possible for the distance optimal planning to not violate the MTR constraint, for example if the vehicle is initially pointed towards the goal, in which case it will move in a trajectory with very large radii of curvature; however, the experiments cited here did not involve this situation.) In contrast energy efficient motion planning enforced the MTR constraint and reduced the energy consumption by an average of 38.85% while increasing the distance traveled by an average of only 4.3%. Furthermore, the average computational time for computing a distance optimal trajectory was in the range $[0.007, 0.566]sec$ and averaged $0.171sec$, while the computational times for the energy efficient trajectories were in the range $[0.007, 1.635]sec$ and averaged $0.217sec$. Although the energy efficient trajectories had the higher average computational time, for a given scenario they were not always more computationally expensive. The higher times appeared to be due to the enforcement of the MTR constraints, which sometimes forced SBMPO to search the input space more in order to find an input leading to a feasible trajectory. However, the MTR constraint can also cause the vehicle to find a trajectory that avoids obstacles, instead of weaving through them, which can lead to smaller computational times.

### 4.3 Experimental Results for a Wooden Surface

This section describes and discusses the results of experiments conducted on a $7m \times 7m$ flat wooden surface. Each of the energy efficient trajectories and each of the distance optimal trajectories, corresponded to the FSU-Bot moving at a constant forward velocity of $0.2m/s$. The experimental results discussed here[2] and below in Section 4.4 (for movement on asphalt) highlight the importance of the MTR constraint, since it cannot be ignored as it was in the simulation results of the previous section. In particular, they provide concrete illustration of the difficulties in attempting to track trajectories designed without taking into account this constraint. They also give insight into the accuracy of the energy consumption predicted by the power model.

The tracking results for the robot are shown in Figs. 16−18 for Scenario 2, and in Figs. 19−21 for Scenario 3. Figs. 16 and 19 show the position tracking of the robot using a Vicon motion capture system for both distance optimal and energy efficient trajectories. Figs. 18 and 21 show the velocity tracking and torque measurement of the robot while executing the energy efficient trajec-

[2] This paper has supplementary downloadable material (Motion_planning.zip) showing the motion planning results for movement on both wood and asphalt surfaces as presented in this paper.

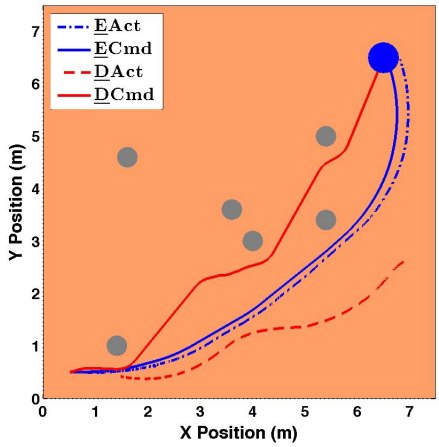


**Fig. 16** Motion planning results for Scenario 2 with 0° initial heading with respect to the $x$-axis, start at $(0.5, 0.5)m$, goal at $(6.5, 6.5)m$, and no payload ($\underline{E}$ represents energy optimal trajectories and $\underline{D}$ represents distance optimal trajectory.) The experiments was conducted on a flat wooden surface with a commanded constant forward velocity of $0.2m/s$. The robot was not able to track the distance optimal trajectory and headed away from the goal. For the energy optimal trajectory, the tracking was good and the robot was able to reach the goal.

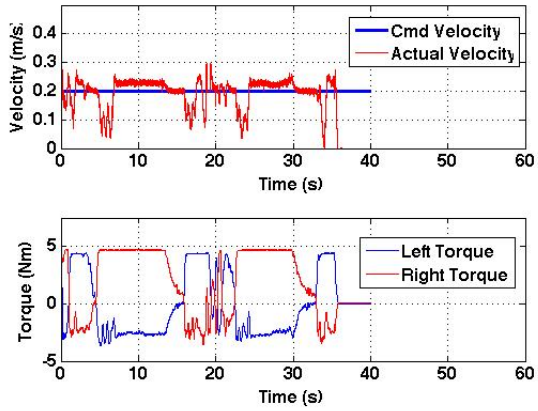


**Fig. 17** Velocity tracking and torque measurement results for the distance optimal trajectory shown in Fig. 16. The vehicle was not able to track the velocity due to torque saturation.

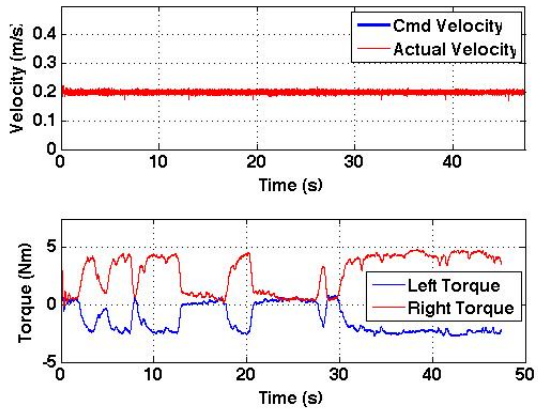


**Fig. 18** Velocity tracking and torque measurement results for the energy optimal trajectory shown in Fig. 16. The vehicle was able to avoid saturating the two actuators and had good velocity tracking.

tories of Scenarios 2 and 3, respectively. As shown in these figures, the robot was able to properly track the energy efficient trajectories. The experimental results are shown in Table 4 along with the simulated results. For distance optimal trajectories, the robot trajectory tracking was significantly off. As shown in Figs. 17 and 20, most of the time the robot actuators were saturated, causing poor velocity and position tracking as seen in Fig. 16 for Scenario 2 and Fig. 19 for Scenario 3. In Table 4, some cells are labeled as "N.A.", indicating that the vehicle did not complete the mission by either hitting an obstacle or moving significantly off course.

The experiments were further extended to study the effect of payload on the motion planning task. In Scenario 4, the robot was first commanded with a no payload, energy efficient trajectory. As can be seen from Fig. 22, the robot was able to closely track the trajectory with an actual energy consumption of $348J$ and a predicted energy consumption of $471J$. The robot was then commanded with the same trajectory but while carrying a payload of $8kg$. The position tracking results are shown in Fig. 22 with velocity tracking and torque measurements in Fig. 23. As can be seen from Fig. 23 the actuators of the robot were saturated, causing poor velocity tracking and leading to collision with an obstacle. However, when the robot having an $8kg$ payload was commanded with an $8kg$ energy efficient trajectory, it was able to avoid obstacles and reach the goal. It should be noted that the small error in the final position of the robot could be due to an error in the initial orientation of the robot.

Fig. 24 shows the percentage error in the energy prediction for 17 combinations of payloads and obstacle configurations for energy efficient motion planning on wood and asphalt. For each scenario, the error was averaged over three experimental runs. As can be seen in the Fig. 24 , the maximum error was $-35.25\%$, the minimum error was $-5.90\%$, and the mean error was $-19.88\%$ for the different scenarios. This over-prediction of energy consumption is partly due to the fact that the predicted torques tend to be greater than the experimental torques as evidenced in Figs. 7−12, leading to an over-prediction of power. Integration of the small error in power over time leads to significant errors in the prediction of energy. The higher errors

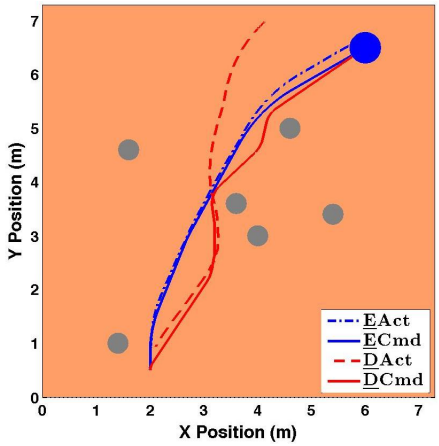


**Fig. 19** Motion planning results for Scenario 3 with 90° initial heading with respect to the $x$-axis, start at $(2.0, 0.5)m$, goal at $(6.0, 6.5)m$, and no payload ($\underline{E}$ represents energy optimal trajectories and $\underline{D}$ represents distance optimal trajectory.) The experiment was conducted on a flat wooden surface with a commanded constant forward velocity of $0.2m/s$. The robot was not able to track the distance optimal trajectory and headed away from the goal. For the energy optimal trajectory, the tracking was good and the robot was able to reach the goal.

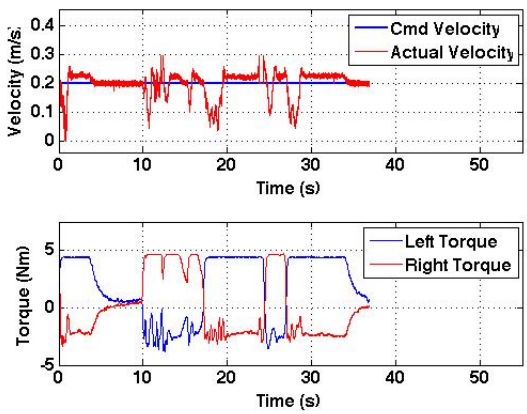


**Fig. 20** Velocity tracking and torque measurement results for the distance optimal trajectory shown in Fig. 19. The vehicle was not able to track the velocity due to torque saturation.

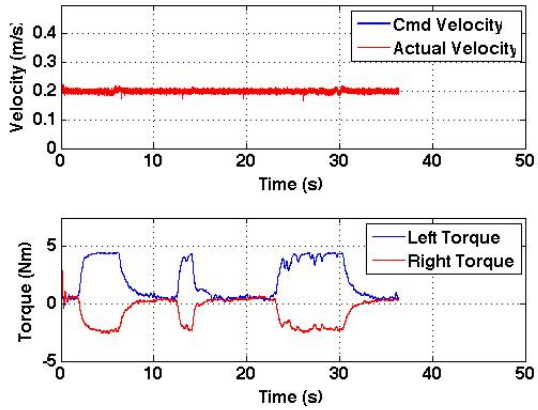


**Fig. 21** Velocity tracking and torque measurement results for the energy optimal trajectory shown in Fig. 19. The vehicle was able to avoid saturating the two actuators and had good velocity tracking.

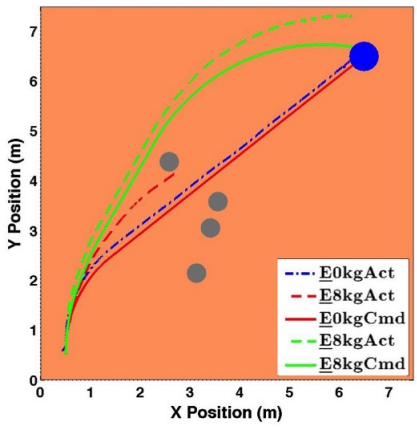


**Fig. 22** Motion planning results for Scenario 4 with 90° initial heading with respect to the $x$-axis, start at $(0.5, 0.5)m$, goal at $(6.5, 6.5)m$, and various payloads ($\underline{E}$ represents energy optimal trajectories). The experiment was conducted on a flat wooden surface with a commanded constant forward velocity of $0.2m/s$. The robot carried an $8kg$ payload but the commanded energy optimal trajectory assumed no payload and the robot was not able to track the trajectory and even hit an obstacle.

seen for the wooden surface are likely due to the anisotropic nature of this surface, which contrasts with the relatively isotropic nature of the asphalt surface. (Experimental results for the asphalt surface are discussed in Section 4.4.) It should be emphasized that the dynamic model described in Section II-B assumes an isotropic surface since the surface parameters ($\mu_o$, $\mu_i$ and $K$) are constant. To account for anisotropy, these parameters must vary according to the vehicle orientation with respect to the surface. This makes the model (and its use) more complex and in practice, would also require a perception system that can detect the grain direction or other directional properties of the surface.

Table 4 shows the computational times for both distance optimal and energy efficient motion planning. As can be seen from the table, the computational times for energy efficient motion planning ranged from 0.011 sec to 1.64 sec and were comparable with the corresponding times (when they exist) for the distance optimal trajectories.

**Table 4** Experimental results for motion planning

| Scenario | Planning | | Comp. Time (s) | Path Length (m) | Pred. Energy (J) | Actual Energy (J) | Error % |
|---|---|---|---|---|---|---|---|
| 2. | Min. Dist. | | 0.5554 | 8.9 | 1276 | N.A. | N.A. |
| | Min. Energy | | 0.8798 | 9.5 | 854 | 765.17 | -11.61 |
| 3. | Min. Dist. | | 0.5664 | 7.3 | 935 | N.A. | N.A. |
| | Min. Energy | | 0.186 | 7.4 | 489 | 387 | -26.34 |
| 4. | Min. Energy. | | | | | | |
| | Payload | | | | | | |
| | Assumed | Actual | | | | | |
| | $0kg$ | $0kg$ | 0.0107 | 8.5 | 471 | 348 | -35.25 |
| | $0kg$ | $8kg$ | 0.0107 | 8.5 | 471 | N.A. | N.A. |
| | $8kg$ | $8kg$ | 1.6353 | 9.4 | 1122 | 927 | -20.98 |
| 5. | Min. Dist. | | 0.042 | 11.46 | 843 | N.A. | N.A. |
| | Min. Energy | | 0.125 | 12.06 | 507 | 439 | -15.55 |
| 6. | Min. Energy. | | | | | | |
| | Payload | | | | | | |
| | Assumed | Actual | | | | | |
| | $0kg$ | $0kg$ | 0.1509 | 11.76 | 511 | 419 | -21.96 |
| | $0kg$ | $8kg$ | 0.1509 | 11.76 | 511 | N.A. | N.A. |
| | $8kg$ | $8kg$ | 0.024 | 12.48 | 749 | 622 | -20.42 |

⋆N.A. = Not applicable if the vehicle hits an obstacle or headed away from the goal.

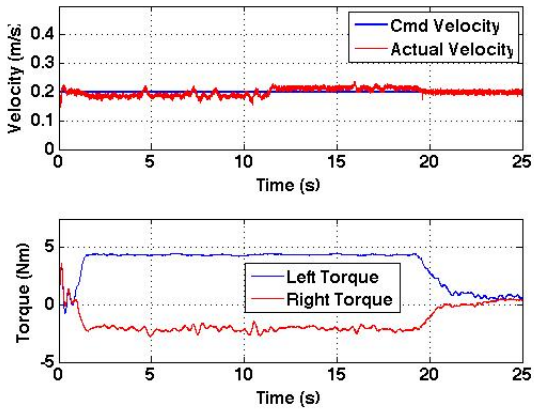


**Fig. 23** Velocity tracking and torque measurement results with the robot carrying an $8kg$ payload but commanded to follow the $0kg$ payload energy optimal trajectory shown in Fig. 22. The vehicle was not able to track the velocity due to torque saturation.

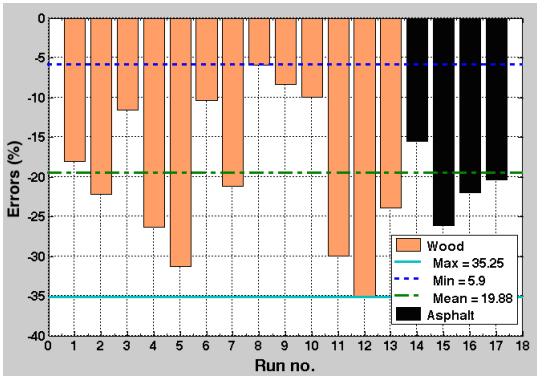


**Fig. 24** The graph of the error ($\frac{E_{act}-E_{pred}}{E_{act}}$), where $E_{act}$ and $E_{pred}$ are respectively the actual and predicted energy consumption, for the robot executing various energy optimal trajectories on the wood and asphalt surfaces.

## 4.4 Experimental Results for Asphalt Surface

The results of Section 4.3 were later extended to an outdoor asphalt surface with the robot moving at the higher speed of $0.6m/s$. First, the dynamic model for FSU-Bot was verified for a constant forward velocity of $0.6m/s$ and the results are shown in Fig 25. It should be noted that the surface parameters were maintained at the same values identified for the robot running at a constant forward velocity of $0.2m/s$ on the asphalt surface. Then, simulation and experimental motion planning was performed for the FSU-Bot running at a constant forward velocity of $0.6m/s$. The motion planning results for Scenario 5 and Scenario 6 are shown in Figs. 26 and 27, respectively and the computational time comparison is shown in Table 4. The high quality of the MTR and energy prediction results here strongly suggests that the dynamic and power model have low dependence on the vehicle speed.

Fig. 26 shows the position tracking of the FSU-Bot while following the energy efficient and distance optimal trajectories for Scenario 5 at a constant forward velocity of $0.6m/s$. As shown in this figure, the robot was able to track the energy efficient trajectory. In contrast, while tracking the distance optimal trajectory, the left actuator saturated during sharp turns, causing the robot to hit an obstacle. The total actual energy for the energy efficient trajectory was $439J$ as compared to the total predicted energy of $507J$ with an error of

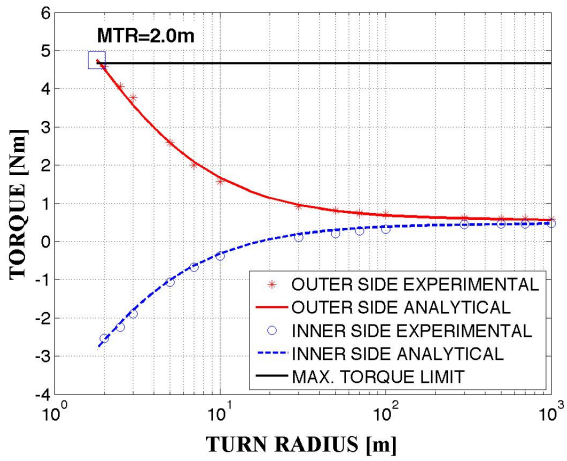


**Fig. 25** Torque vs. Turn Radius curve for the FSU-Bot with no payload on a flat asphalt surface running at a constant forward velocity of $0.6m/s$. The expansion factor and surface parameters were maintained at the same values as those identified with no payload and a constant forward velocity of $0.2m/s$. The minimum turn radius ($MTR$) for no payload is $2.0m$.

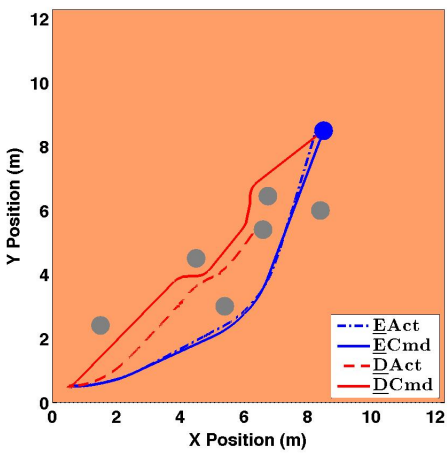


**Fig. 26** Motion planning results for Scenario 5 with 0° initial heading with respect to the $x$-axis, start at $(0.5, 0.5)m$, goal at $(8.5, 8.5)m$, and no payload ($\underline{E}$ represents energy optimal trajectories and $\underline{D}$ represents distance optimal trajectory.) The experiment was conducted on an asphalt surface with a commanded constant forward velocity of $0.6m/s$. The robot was not able to track the distance optimal trajectory and actually hit an obstacle. For the energy optimal trajectory, the robot was able to track the trajectory and reach the goal.

$-15.55\%$. Since the robot hit an obstacle while tracking the distance optimal trajectory of Scenario 5 (see Fig. 26), the total actual energy measurement was not applicable here.

Experiments were also conducted to test the effect of payload while tracking the energy efficient trajectory on the asphalt surface. First, the robot was commanded to follow the energy efficient trajectory with no payload

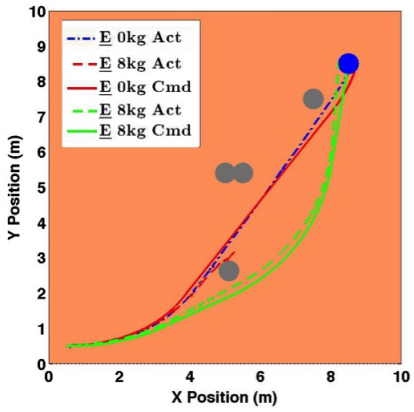


**Fig. 27** Motion planning results for Scenario 6 with 0° initial heading with respect to the $x$-axis, start at $(0.5, 0.5)m$, goal at $(8.5, 8.5)m$, and various payload ($\underline{E}$ represents energy optimal trajectories). The experiment was conducted on an asphalt surface with a commanded constant forward velocity of $0.6m/s$. The robot carried an $8kg$ payload but was commanded to follow a $0kg$ payload energy optimal trajectory and hit an obstacle.

for Scenario 6, as shown in Fig. 27. The total actual energy was $419J$ in comparison to the predicted energy of $511J$ with an error of $-21.96\%$. Then, the robot was commanded with the same trajectory but having an actual payload of $8kg$. As can be seen in Fig. 27, the robot was not able to track the trajectory and eventually hit an obstacle. However, when the robot having an $8kg$ payload was commanded with an $8kg$ payload trajectory, it was able to track the trajectory (shown in Fig. 27). The total actual energy was $622J$ in comparison to the total predicted energy of $749J$ with an error of $-20.42\%$.

## 5 Extension to Motion Planning on Slopes

The results of Section 4.3 were limited to flat surfaces. However, using the 3D dynamic model Ordonez et al (2012b), the work presented here can be extended to motion planning on slopes. The power model in (12) is basically a function of torque, which for constant velocity motion on a given sloped terrain depends on vehicle orientation and the turn radius. For energy efficient motion planning on a slope, the heuristic function of (18) will have non-zero potential energy ($mgh$). Energy efficient motion planning can be achieved following the same methodology developed earlier in the paper.

Fig. 28 shows a preliminary result for 3D energy efficient motion planning along with a comparison with distance optimal motion planning on a 10° inclined wooden surface. The robot was made to move from the $(0, 0, 0)m$ start position, an initial orientation $\theta_o = 90°$

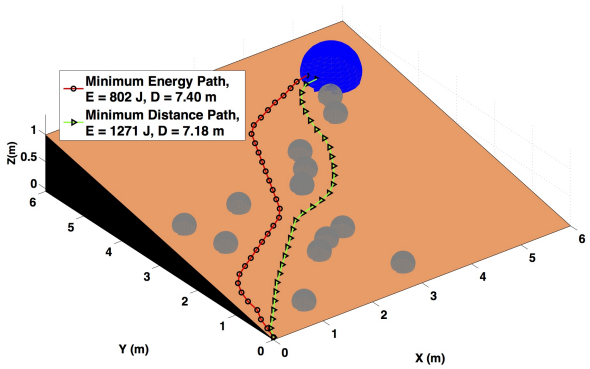


**Fig. 28** Simulated motion planning results for a cluttered environment with $90^o$ initial heading with respect to the $x$-axis, start at $(0, 0, 0)m$, goal at $(5.0, 5.0, 0.87)m$, and no payload. The terrain has an inclination of $10^o$ and the robot was commanded with a constant forward velocity of $0.2m/s$.

to the goal region, centered at $(5.0, 5.0, 0.87)m$, while avoiding obstacles. As can be seen from the figure, for the energy efficient trajectory, the robot avoided sharp turns and moved as straight as possible. However, for the distance optimal trajectory, the robot made a sharp turn at the start point $(0, 0, 0)m$. The total energy consumption for the energy efficient trajectory turned out to be $802J$ for a total path length of $7.40m$, whereas for the distance optimal path it was $1271J$ for a total path length of $7.18m$. Hence, a 36.8% decrease in energy consumption was achieved with only a 3.1% increase in distance traveled.

## 6 Conclusions

This paper considered autonomous skid-steered wheeled vehicles. The focus has been the efficient computation and evaluation of trajectories that are dynamically feasible (i.e., they obey a minimum turn radius (MTR) constraint) and energy efficient. These trajectories were compared in both simulation and experiments with more standard distance optimal trajectories. The results relied upon dynamic and power models for skid-steered wheeled vehicles, discussed respectively in Sections 2.2 and 2.3, and their use with Sampling Based Model Predictive Optimization (SBMPO), the motion planning algorithm of Section 3. The key contributions are the validation of the models for different payloads and speeds, their integration with the planner and the insights that have been developed in performing the simulations and experiments.

An interesting and useful experimental result, revealed in Section 4.1, is that the surface parameters appearing in the dynamic model of the vehicle, i.e., the coefficients of friction for the inner and outer wheels ($\mu_i$ and $\mu_o$) and the shear deformation modulus $K$ can be experimentally identified when the vehicle is not carrying a payload, but will yield fairly accurate predictions of torque when the vehicle is carrying a substantial payload. Hence, these parameters do not have to be re-identified when the vehicle's payload increases.

The simulation results of Section 4.2 reveal particular insights for skid-steered vehicles that distance optimal trajectories, if they can be followed by the robot, can be very energy consuming, primarily. In contrast the dynamically feasible, energy efficient trajectories tend to require the vehicle to have a slight increase (an average of 4.3% in the simulations) in distance and time traveled, but lead to a dramatic decrease (an average of 38.8% in the simulations) in energy consumed. These results revealed that when energy conservation for skid-steered autonomous ground vehicles is important, for example, to increase a mission's endurance, energy efficient motion planning can be critical.

Because most of the distance optimal trajectories violated the corresponding MTR constraint, the experimental results of Section 4.3 particularly highlighted the importance of enforcing these constraints in order to enable successful trajectory tracking. Without this enforcement, it is easy to develop trajectories that the vehicle simply cannot follow. It is pertinent to emphasize that in our control system, the company-specified current (i.e., torque) limits of each of the vehicle's two motors is enforced by each motor's controller. However, it is possible to violate these current limits at the risk of burning out one or more of the motors. Hence, if the current limit was not rigorously enforced, the vehicle may have been able to track the distance optimal trajectories, albeit at great risk. The contention here is that this would be very poor practice.

Initial simulation results were shown in Section 5 for energy efficient motion planning on a slope. A focus of future work will be energy efficient planning in environments with variable and slippery slopes. In such scenarios, it is expected that the current kinematic model will have to be enhanced with more detailed slip models such as those of Seegmiller et al (2013).

Other important areas of future work are motion planning for heterogeneous surfaces and rapid re-planning of energy efficient trajectories. As is well known, in a real world scenario a robot must update its plans to take into account new environmental information and differences between its current state and predicted state. It is possible to develop and implement an incremental version of SBMPO that will enable this rapid re-planning and this work is underway.

**Acknowledgements** This work was supported by the collaborative participation in the Robotics Consortium sponsored by the U.S. Army Research Laboratory under the Collaborative Technology Alliance Program, Cooperative Agreement DAAD 19-01-2-0012. The U.S. Government is authorized to reproduce and distribute reprints for Government purposes not withstanding any copyright notation thereon.

## References

Barili A, Ceresa M, Parisi C (1995) Energy saving motion control for an autonomous mobile robot. In: Proceedings of the International Symposium on Industrial Electronics, pp 674–676

Caldwell C, Dunlap D, Collins EGJ (2010) Motion planning for an autonomous underwater vehicle via sampling based model predictive control. In: OCEANS 2010, pp 1–6

Caracciolo L, De Luca A, Iannitti S (1999) Trajectory tracking control of a four-wheel differentially driven mobile robot. In: Robotics and Automation, 1999. Proceedings. 1999 IEEE International Conference on, vol 4, pp 2632–2638 vol.4

Chuy O, Collins E, Dunlap D, Sharma A (2013) Sampling-based direct trajectory generation using the minimum time cost function. In: Experimental Robotics, Springer Tracts in Advanced Robotics, vol 88, Springer International Publishing, pp 651–666

Collins E, Yu W, Chuy O, Gupta N (2011) Dynamic and power modeling for skid-steered vehicles. In: NSF Engineering Research and Innovation Conference

Dunlap D, Yu W, Collins J EG, Caldwell C (2011a) Motion planning for steep hill climbing. In: Robotics and Automation (ICRA), 2011 IEEE International Conference on, pp 707–714

Dunlap DD, Caldwell CV, Collins EGJ (2010) Nonlinear model predictive control using sampling and goal-directed optimization. In: IEEE Conference on Control Applications, pp 1349–1356

Dunlap DD, Caldwell CV, Collins EGJ, Chuy O (2011b) Motion Planning for Mobile Robots Via Sampling-Based Model Predictive Optimization. Intech

Dyer C (2002) Fuel cells for portable applications. Fuel Cell Bulletin pp 8–9

Ericson C (2005) Real-Time Collision Detection. Elsevier

Hwang Y, Ahuja N (1992) Gross motion planning - a survey. ACM Computing Surveys pp 219–291

Karaman S, Frazzoli E (2011) Sampling-based algorithms for optimal motion planning. The International Journal of Robotics Research 30(7):846–894

Kozlowski K, Pazderski D (2004) Modeling and control of a 4-wheel skid-steering mobile robot. International Journal of Mathematics and Computer Science pp 477–496

Likhachev M, Ferguson D (2009) Planning long dynamically feasible maneuvers for autonomous vehicles. The International Journal of Robotics Research 28(8):933–945

Mandow A, Martinez J, Morales J, Blanco JL, Garcia-Cerezo A, Gonzalez J (2007) Experimental kinematics for wheeled skid-steer mobile robots. In: Intelligent Robots and Systems, 2007. IROS 2007. IEEE/RSJ International Conference on, pp 1222–1227

Martnez JL, Mandow A, Morales J, Pedraza S, Garca-Cerezo A (2005) Approximating kinematics for tracked mobile robots. The International Journal of Robotics Research 24(10):867–878

Mei Y, Lu YH, Hu Y, Lee CSG (2004) Energy-efficient motion planning for mobile robots. In: Robotics and Automation, 2004. Proceedings. ICRA '04. 2004 IEEE International Conference on, vol 5, pp 4344–4349 Vol.5

Mei Y, Lu Y, Hu Y, Lee C (2006) Deployment of mobile robots with energy and timing constraints. IEEE Transactions on Robotics

Moosavian S, Kalantari A (2008) Experimental slip estimation for exact kinematics modeling and control of a tracked mobile robot. In: Intelligent Robots and Systems, 2008. IROS 2008. IEEE/RSJ International Conference on, pp 95–100

Ordonez C, Gupta N, Collins Jr EG, Clark JE, Johnson AM (2012a) Power modeling of the xrl hexapedal robot and its application to energy efficient motion planning. In: Proceedings of the 15th International Conference on Climbing and Walking Robots and the Support Technologies for Mobile Machines, World Scientific, vol 23, p 26

Ordonez C, Gupta N, Yu W, Chuy O, Collins E (2012b) Modeling of skid-steered wheeled robotic vehicles on sloped terrains. In: Proceedings of the ASME Dynamic Systems and Control Conference, pp 91–99

Ordonez C, Gupta N, Chuy O, Collins EG (2013) Momentum based traversal of mobility challenges for autonomous ground vehicles. In: Robotics and Automation (ICRA), 2013 IEEE International Conference on, pp 752–759

Perez T, Wesley M (1979) An algorithm for planning collision-free paths among polyhedral obstacles. Communications of the ACM pp 560–570

Reese B (2015) A graph based approach to nonlinear model predictive control with application to combustion control and flow control. PhD thesis, Florida State University, Tallahassee, FL

Schwartz J, Sharir M (1988) A survey of motion planning and related geometric algorithms. Artificial Intelligence Journal

Seegmiller N, Rogers-Marcovitz F, Miller G, Kelly A (2013) Vehicle model identification by integrated prediction error minimization. The International Journal of Robotics Research 32(8):912–931

Tekscan (2010) Tire footprint pressure measurement. http://www.tekscan.com/industrial/tirescan-system.html

Wong JY (2001) Theory of Ground Vehicles, 3rd edn. John Wiley & Sons, Inc

Wong JY, Chiang CF (2001) A general theory for skid steering of tracked vehicles on firm ground. In: Proceedings of the Institution of Mechanical Engineers, Part D, Journal of Automotive Engineerings, pp 343–355

Yi J, Song D, Zhang J, Goodwin Z (2007) Adaptive trajectory tracking control of skid-steered mobile robots. In: Proceedings of the International Conference on Robotics and Automation, Roma, Italy, pp 2605–2610

Yi J, Wang H, Zhang J, Song D, Jayasuriya S, Liu J (2009) Kinematic modeling and analysis of skid-steered mobile robots with applications to low-cost inertial-measurement-unit-based motion estimation. Robotics, IEEE Transactions on 25(5):1087–1097

Yu W, Chuy O, Collins EG, Hollis P (2010) Analysis and experimental verification for dynamic modeling of a skid-steered wheeled vehicle. IEEE Transactions on Robotics pp 340–353

Yu W, Collins E, Chuy O (2011) Dynamic Modeling and Power Modeling of Robotic Skid-Steered Wheeled Vehicles,. Intech